

Origin and reduction of wakefields in photonic crystal accelerator cavities

Carl A. Bauer,¹ Gregory R. Werner,¹ and John R. Cary^{1,2}

¹University of Colorado at Boulder, Boulder, CO

²Tech-X Corporation, Boulder, CO

(Dated: June 11, 2022)

Photonic crystal (PhC) defect cavities that support an accelerating mode tend to trap unwanted higher-order modes (HOMs) corresponding to zero-group-velocity PhC lattice modes at the top of the bandgap. The effect is explained quite generally by photonic band and perturbation theoretical arguments. Transverse wakefields resulting from this effect are observed in a hybrid dielectric PhC accelerating cavity based on a triangular lattice of sapphire rods. These wakefields are, on average, an order of magnitude higher than those in the waveguide-damped Compact Linear Collider (CLIC) copper cavities. The avoidance of translational symmetry (and, thus, the bandgap concept) can dramatically improve HOM damping in PhC-based structures.

I. INTRODUCTION

Photonic crystals (PhCs) have recently attracted interest from the accelerator community [1–12] for the following reasons:

1. PhCs enable the construction of accelerator cavities using dielectric materials.
2. PhC cavities intrinsically provide a wakefield damping mechanism.

These features suggest an alternative to traditional (super)conducting cavity design, and therefore *could* result in higher gradients [13–17], lower power losses, and/or lower wakefields.

A simple argument from photonic band theory gives reason to believe that PhC cavities will have low wakefields. It says that, given a PhC with a bandgap, a defect cavity will confine only one (ideally accelerating) mode to the defect; all other higher-frequency modes will propagate through the crystal and contribute minimally to the wakefields. This basic concept has led to the design of many defect cavity PhC acceleration schemes, a sample of which can be seen in the list of references above.

To date, only a handful of computational and experimental studies dedicated to wakefield damping in PhC cavities have been performed. In general, they have shown that the Q-factors of higher-order modes (HOMs) are much lower than that of the accelerating mode, indicating some wakefield damping [18–20]. These studies were performed on so-called hybrid PhC cavities (at GHz frequencies), where “hybrid” indicates the incorporation of both PhC *and* traditional (metal disc-loaded waveguide) design concepts (look ahead to Fig. 4 for an example of a hybrid PhC cavity) [2, 3, 8].

This work looks in more detail at wakefield suppression in PhC cavities and reveals subtleties that can undermine the benefits implied by the simple bandgap argument. These subtleties were uncovered in a thorough comparison between wakefield damping in a hybrid PhC cavity based on a triangular lattice of sapphire rods (Fig. 4) and a cavity from the main linac of the Compact Linear

Collider (CLIC) which uses side-coupled waveguides to damp HOMs (see Fig. 1) [21–24].

We find that, in the case of the hybrid PhC cavity (with sapphire rods) based on the triangular lattice, transverse wakefields are on average higher than those in the CLIC waveguide-damped cavity. A simple Fourier analysis of the transverse wake potential compared with the triangular lattice band diagram shows that the band edges (where the dispersion curves flatten) are highly correlated with troublesome peaks in the transverse wake impedance. We attribute this correlation to the slow rate at which low-group-velocity PhC modes transport energy through the lattice.

We also find that PhC-based cavities optimized to confine the accelerating mode with a minimal number of rods can reduce wakefields compared to a PhC lattice cavity with similar accelerating mode Q-factor. The results of this paper show that the bandgap property of PhC-based cavities is not enough to guarantee ideal wakefield suppression. Given the configurability of PhCs (and our previous work in Ref. [10]), we suggest minimizing wakes through rod-placement optimization.

The following two sections review waveguide and PhC wakefield damping techniques. Section IV describes our simulation methods and results, comparing wakefields in the CLIC and lattice-based hybrid dielectric PhC cavities. Section V discusses the poor damping found in the triangular-lattice-based PhC cavity using photonic band theory. Finally, Section VI repeats the simulations of Section IV with an optimized cavity (from Ref. [10]) and compares these results with CLIC. Appendix A analyzes the performance of our numerical absorbers used in wakefield simulations. Appendix B discusses accelerating mode figures of merit (peak surface fields, accelerating efficiency, etc.) for each cavity type considered in this work.

II. WAVEGUIDE DAMPING AND CLIC

In the waveguide damping technique, wakefields are reduced by coupling HOMs out through waveguides ter-

minated by electromagnetic absorbers. The CLIC design includes four radially-directed waveguides in every cell, optimized to damp the TM_{110} cavity mode (since the TM_{110} mode, or lowest dipole mode, is the largest contributor to transverse wakefields). Figure 1 shows the second cell of the 26-cell constant-gradient CLIC cavity, TD26_vg1.8_R05_CC [24] (the second cell is the first “regular” cell, i.e. the first cell *without* power input couplers). The multicell cavity is formed by stacking pieces similar to that shown in Fig. 1.

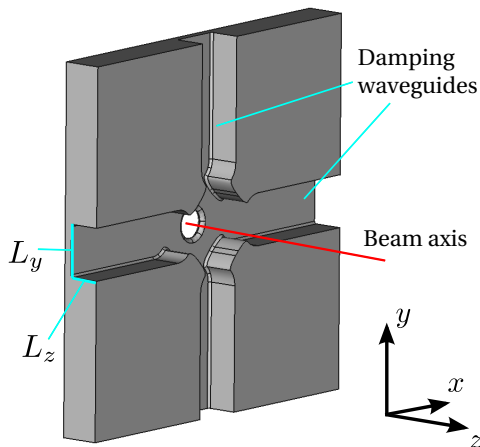


FIG. 1: In the above CLIC accelerating cell, [25] the four radial rectangular waveguides (terminated by electromagnetic absorbers) strongly damp HOMs; the cutoff frequency of each waveguide is slightly above the accelerating mode frequency and well below the lowest dipole frequency.

The waveguides of the CLIC cavity effectively damp the lowest dipole mode (and other HOMs) *without* damping the accelerating mode. This desired behavior was obtained by carefully selecting the waveguide cross-section such that the lowest waveguide cutoff frequency is between the accelerating mode and (undamped) dipole mode frequencies. For the CLIC cell in Fig. 1, the lowest waveguide cutoff frequency is $c/2L_y = 13.6$ GHz ($L_y = 11$ mm), the accelerating mode frequency is 12 GHz, and the frequency of an undamped dipole mode (i.e. dipole mode in a CLIC cell *without* damping waveguides) is approximately 21 GHz. Since the frequency of the accelerating mode is below waveguide cutoff, the mode remains confined to the cavity; the dipole mode, however, is free to propagate down the waveguides. The cutoff frequency is chosen far below the undamped dipole frequency because damping is less effective near cutoff where the group velocity (and thus speed of energy transport) of the waveguide mode vanishes [26, 27].

III. INTRINSIC DAMPING IN PHCS

Photonic crystals offer an alternative approach to wakefield damping: confine only the accelerating mode.

This approach is made possible by the bandgap property of some PhCs, and the resulting defect-mode phenomenon. A brief overview follows.

A *band diagram* succinctly summarizes the electromagnetic properties of PhCs. It is well-known from Bloch theory that electromagnetic eigenmodes in periodic structures take the form

$$\mathbf{E}(\mathbf{x}, t) = \tilde{\mathbf{E}}_n(\mathbf{x})e^{i\mathbf{k}\cdot\mathbf{x} - i\omega_n(\mathbf{k})t} \quad (1)$$

where the reciprocal lattice vector \mathbf{k} runs over a reduced region of k -space called the first Brillouin zone, n is an integer indexing “bands” of solutions, and $\tilde{\mathbf{E}}_n$ has the periodicity of the lattice. A band diagram traditionally plots the resonant frequencies ω_n in each band along a representative k -space path within the first Brillouin zone. Figure 2c shows the TM band diagram for the PhC of interest to this paper (2D triangular lattice of sapphire discs—shown in Fig. 2a) along the k -space path shown in Fig. 2b.

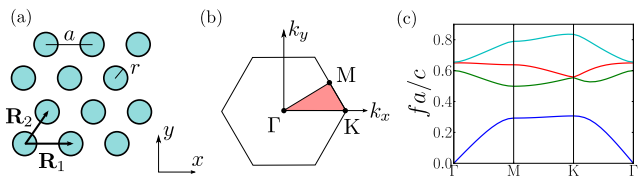


FIG. 2: Propagation in the 2D triangular lattice of sapphire discs (a) is forbidden for TM electromagnetic waves with frequencies near $0.4c/a$ because of the bandgap (c). Lattice vectors \mathbf{R}_1 and \mathbf{R}_2 , inter-disc spacing a , and disc radius r are defined in (a). The first Brillouin zone of the reciprocal lattice is identified in (b) by the hexagon; the *irreducible* Brillouin zone is shaded and represents the entire Brillouin zone by symmetry. The dispersion curves for the first 4 bands along the path outlining the shaded region in (b) are shown in (c) for $r = 0.17a$. Calculations were performed using the MIT Photonic Bands simulation code [28].

Of central importance in Fig. 2c is the wide range of frequencies between the first and second band in which there are no solutions. This feature is called a bandgap, and is the basis for the formation of PhC resonant cavities that are of interest to the accelerator community. For a PhC with a bandgap, a resonant cavity can often be formed by removing a single element from the lattice (creating a defect). This introduces a mode that oscillates at a frequency within the bandgap and is necessarily localized to the defect. The defect TM mode for the sapphire triangular lattice is shown in Fig 3 and oscillates at a frequency of $f = 0.41c/a$ —the center of the bandgap; this mode can accelerate particles in/out of the page.

A single cell of a hybrid PhC cavity (Fig. 4) is formed from a 2D PhC of sapphire rods (in this case a triangular lattice) sandwiched between two copper iris plates. As with the CLIC cavity, a multicell version would be assembled by stacking the element shown in Fig. 4.

The dielectric constant of sapphire is anisotropic; in the case of Fig. 4, the c -axis of the sapphire is oriented

along z . This means the dielectric tensor used in our calculations took the form: $\varepsilon = 9.4\varepsilon_0(\hat{x}\hat{x} + \hat{y}\hat{y}) + 11.6\varepsilon_0\hat{z}\hat{z}$ where ε_0 is the vacuum permittivity.

This structure intrinsically damps HOMs because frequencies above the bandgap can propagate through the crystal (assuming no higher-frequency bandgaps). However, as with waveguide damping, one must be wary of flat portions of the dispersion curves, where group velocity (and thus energy transport) vanishes [29]. In the following results and analysis, we find that for the 2D triangular lattice PhC, dipole resonances in the defect are damped poorly by the surrounding PhC. The cause is the coincidence of the dipole resonant frequency with the upper edge of the bandgap, where the second band flattens.

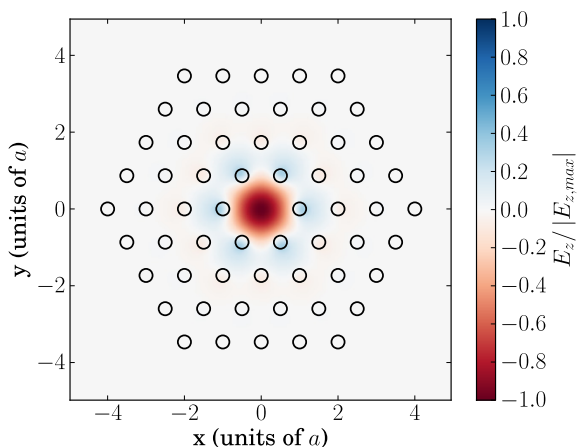


FIG. 3: Resonant TM defect cavity mode in a triangular lattice of lossless sapphire discs ($r = 0.17a$). The lattice is truncated at 4 layers (60 discs), giving a radiative Q -factor of $Q_{\text{rad}} = 24000$. Q_{rad} increases exponentially with the number of layers.

IV. COMPARISON OF WAKEFIELD IN CLIC AND THE TRUNCATED PHC CAVITY

We performed time-domain wakefield simulations for 8-cell versions of the CLIC (Fig. 1) and Tri-4-Sapphire (Fig. 4) cavities [30]. The 8 cells were identical in each cavity type (approximating the behavior of an infinitely periodic single cell). The iris geometry of the Tri-4-Sapphire cavity was matched with the second cell of the TD26_vg1.8_R05_CC cavity, defined by the iris radius $a = 3.15\text{mm}$ and iris thickness $d = 1.67\text{mm}$; as a result, short-range wakefields (those wakefields affecting the drive bunch) are identical in both cavities.

Each cavity was driven by a highly relativistic electron bunch with a Gaussian profile in z , and a delta-function profile in x and y . The Gaussian half-width of the bunch

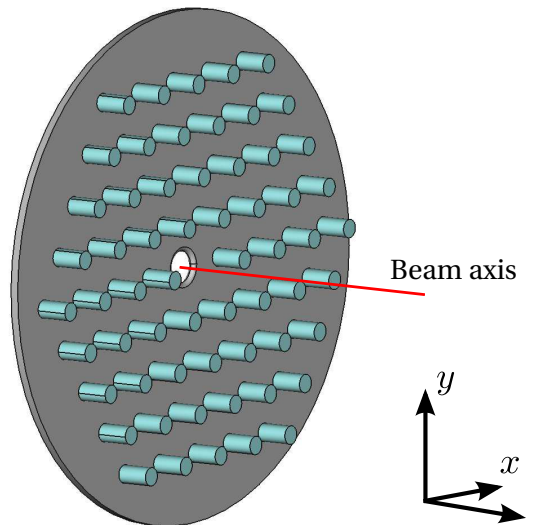


FIG. 4: The triangular lattice PhC of sapphire rods confines the accelerating mode to the beam axis while damping HOMs.

was $\sigma_z = 1\text{mm}$; therefore, HOMs up to frequencies of $\approx 90\text{GHz}$ were excited significantly. To excite transverse wakefields, the bunch was offset (from the beam axis) by 1mm in the x -direction. Wakefields were absorbed by normally conducting layers at the simulation domain boundaries (for further discussion on the performance of these absorbers, see Appendix A).

All simulations were implemented in the VORPAL framework which uses the finite-difference time-domain method for electromagnetics and the particle-in-cell technique for simulating the electron bunch and test particles [31]. In all simulations, grid cells were cubic with $\Delta z = 0.3\text{mm}$ so that the excitation bunch cutoff frequency was simulated with $\approx 10\%$ accuracy.

A. Wake potential

The *wake potential* is the net momentum change (normalized by charge) of a point charge trailing the wakefield excitation bunch. The *longitudinal* wake potential is defined as

$$W_z(s, \mathbf{r}, \mathbf{r}') = -\frac{1}{q_e} \int_0^L E_z(z, \mathbf{r}, \mathbf{r}', t = (s+z)/v) dz \quad (2)$$

where s is the point charge's distance (along z) behind the density peak of the Gaussian excitation bunch, \mathbf{r} is the transverse position of the point charge (the beam axis is the transverse origin), \mathbf{r}' is the transverse position of the excitation bunch, v is the bunch/point charge velocity (basically c), L is the total length of the multicell cavity, and q_e is the excitation bunch charge. Similarly,

the transverse wake potential is defined as

$$\mathbf{W}_\perp(s, \mathbf{r}, \mathbf{r}') = \frac{1}{q_e} \int (\mathbf{E}_\perp + v\hat{z} \times \mathbf{B}_\perp)(z, \mathbf{r}, \mathbf{r}', t = (s+z)/v) dz. \quad (3)$$

In the theoretical case of a cylindrically symmetric cavity with infinitely long beam tubes, the form of the m th-order azimuthal multipole of the wake potential (for $|\mathbf{r}| < a$) is particularly simple [32]:

$$W_{z,m}(r, r', \phi, s) = \partial_s X_m(s) r^m r'^m \cos m\phi \quad (4)$$

$$\mathbf{W}_{\perp,m}(r, r', \phi, s) = m X_m(s) r^{m-1} r'^m (\cos m\phi \hat{r} - \sin m\phi \hat{\phi}) \quad (5)$$

where ϕ' has been set to zero in the above (since only the difference in azimuth matters for cylindrical symmetry) and $m > 0$ for Eq. 5. The transverse wake potential is zero when $m = 0$; only modes with $m > 0$ mediate transverse kicks in this case [32].

The longitudinal and transverse wake potentials are dominated by monopole and dipole wakefields, respectively. The expressions for these contributions are simpler still:

$$W_{z,0} = \partial_s X_0(s) \quad (6)$$

$$\mathbf{W}_{\perp,1} = \mathbf{r}' X_1(s). \quad (7)$$

Both expressions are uniform throughout the beam tube region and the dipole transverse wake potential is proportional to and in the direction of the drive beam's transverse offset.

The structures under consideration are not cylindrically symmetric; nevertheless, the above forms are assumed in our calculations, since the forms hold well for wake potentials near the beam axis [18, 32]. We are mainly interested in the monopole and dipole contributions (i.e. the largest longitudinal and transverse kicks), and therefore plot $\partial_s X_0(s)/L$ and $X_1(s)/L$, in units of V/pC/m and V/pC/m/mm, respectively.

The wake potential was calculated by chasing the drive electron bunch with test particles of very low charge (so that wakefields were not induced by the test particles), but equally diminished mass to retain the electron charge-mass ratio. The net momentum change of the test particles indirectly gives the wake potential. The test particles were organized in rings so that the multipole contributions could be extracted. Six test particles were placed 1 mm from the beam axis.

B. Results

The envelopes (lines connecting local maxima/minima) of the longitudinal monopole wake potentials are shown in Fig. 5 with the corresponding wake impedances shown in Fig. 6. Fluctuations of the envelope give a qualitative picture of the presence of HOMs (showing the full wake potential only serves to

confuse the plot). The impedances in Fig. 6 show lower peaks for the Tri-4-Sapphire cavity, indicating stronger monopole HOM damping and/or weaker monopole HOM excitation. The mode density is significantly higher in Tri-4-Sapphire.

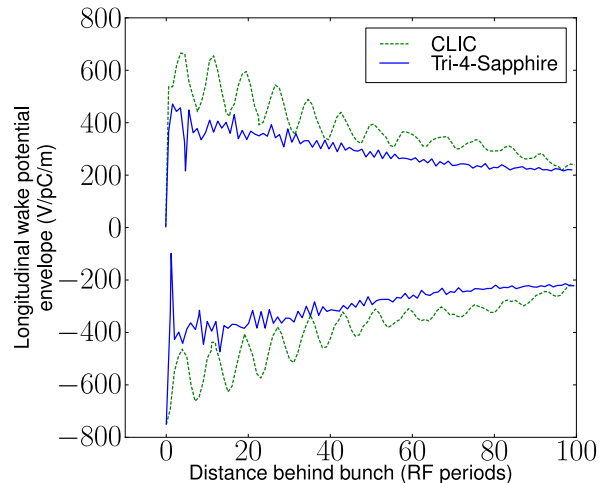


FIG. 5: Oscillations in the envelope of the monopole wake potential indicate the presence of monopole HOMs.

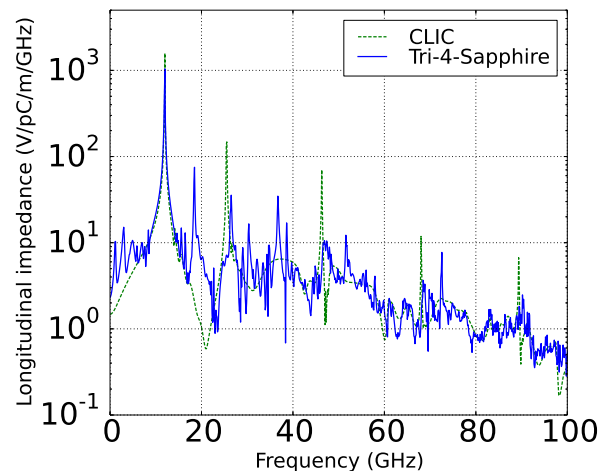


FIG. 6: Monopole HOMs are relatively numerous in the Tri-4-Sapphire cavity, but occur at lower amplitudes.

Amplitudes of the transverse dipole wake potentials are shown in Fig. 7 with the corresponding impedances shown in Fig. 8. As a reference, we have included in each plot the transverse dipole wake potentials in the *empty* cavity—defined most easily as an 8-cell hybrid PhC cavity without *any* rods. The empty cavity represents ideal wakefield damping, but does not confine an accelerating mode. Dipole wakes are relatively high in the Tri-4-Sapphire cavity; the frequencies of the troublesome HOMs are indicated by the sharp peaks around 15 GHz in Fig. 8. This result motivates a more careful

analysis of the intrinsic PhC damping mechanism and prompts the following discussion.

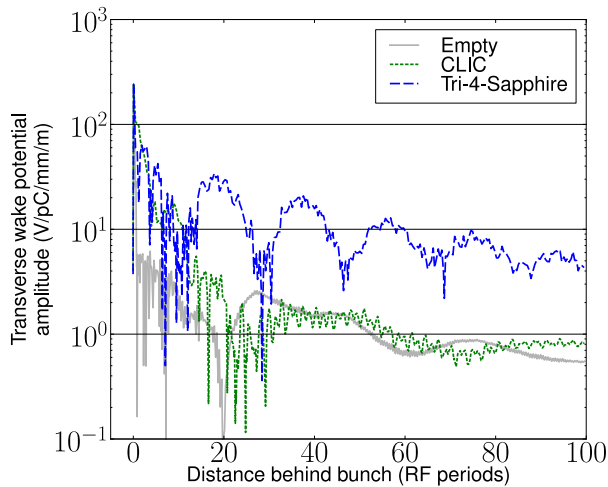


FIG. 7: Transverse dipole wake potentials in the Tri-4-Sapphire cavity are (on average) an order of magnitude higher than those in CLIC.

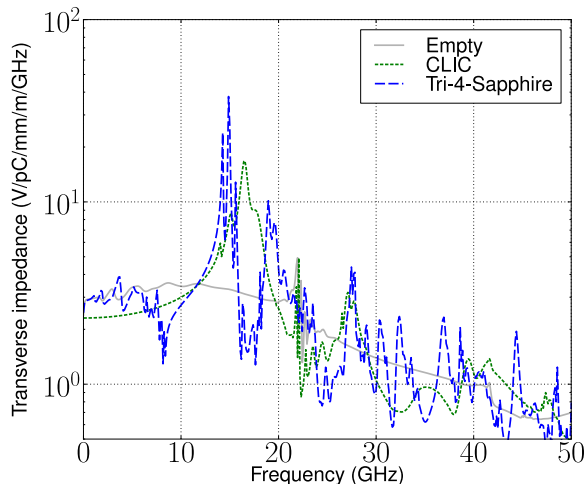


FIG. 8: The higher transverse wake in the Tri-4-Sapphire cavity is due to the cluster of “high”- Q modes around 15 GHz.

V. ORIGIN OF WAKEFIELDS IN THE TRUNCATED PHC CAVITY

The transverse dipole impedance in the Tri-4-Sapphire cavity shows that the dipole wake potential mostly comprises a cluster of modes near 15 GHz. In this section, we explain the presence of these modes using the properties of the triangular-lattice band structure: flat regions of the dispersion diagram imply low-group-velocity PhC modes which sluggishly transport energy and thus cannot effectively damp cavity modes to which they are strongly

coupled. This issue was addressed briefly in Ref. [29] within a study of a square-lattice-based metal-rod accelerating structure.

We have discussed how waveguide damping is effective for coupling out frequencies only above cutoff (the further above cutoff the better). This is because waveguide modes with frequencies near cutoff have vanishing group velocities (because of the flattened dispersion at cutoff) and thus propagate slowly down the waveguide—effectively, they are trapped. In PhCs, the dispersion tends to flatten where the spatial variation of the modes matches the spatial variation of the dielectric, introducing PhC modes with vanishing group velocities.

Figure 9 shows the transverse dipole impedance of the Tri-4-Sapphire cavity in the frequency range 0-25 GHz (a zoom view of Fig. 8) and matches it with the 2D TM band diagram for the triangular lattice of sapphire discs. The two most prominent peaks in the impedance clearly line up with the flat portions of the second band (the third peak can be matched with another flat band in the fully 3D band diagram). The annotated impedance peak (second largest) was investigated further using the time-domain mode extraction technique. Figure 10 shows the field pattern of the extracted mode (from a periodic single-cell simulation at phase advance $\phi \approx 3\pi/4$) and compares it with the 2D PhC lattice mode at the M-point of the second band. The field patterns clearly match.

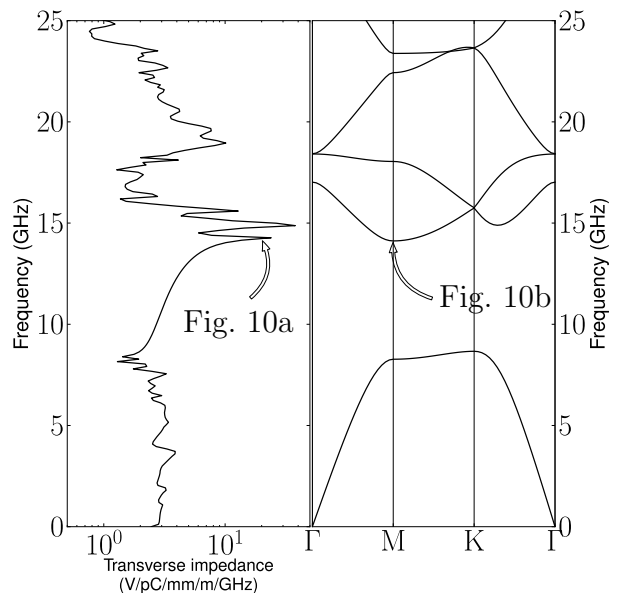
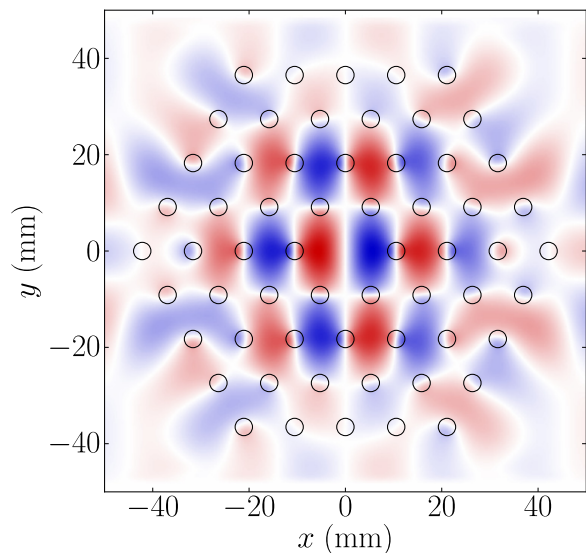
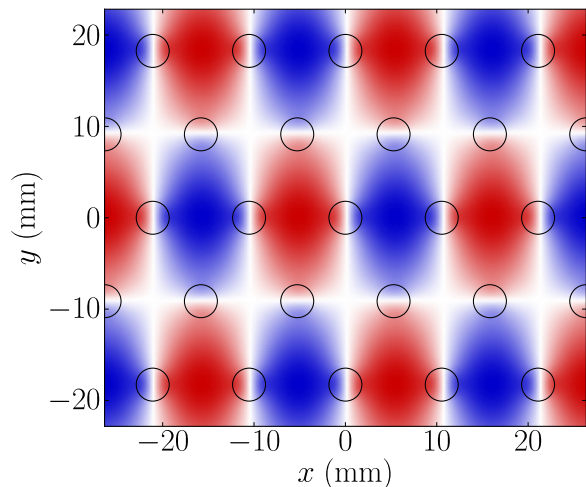


FIG. 9: The left plot shows a zoomed-in view of the troublesome part of the transverse dipole impedance (from Fig. 8). The right plot is the 2D TM band diagram for the triangular lattice of sapphire discs. The annotated peak in the impedance is at the same frequency as the M-point of the second band (also see the mode patterns in Fig. 10). This correlation supports the idea that low- v_g modes pose a problem for wakefields.



(a) Tri-4-Sapphire mode



(b) Infinite PhC mode

FIG. 10: Analogous modes in (a) the Tri-4-Sapphire periodic single-cell cavity and (b) an infinite 2D PhC (the mode pattern in (b) is uniform in z). The propagating PhC mode in (b) has a vanishing group velocity; thus, its counterpart in (a) is “trapped” and contributes significantly to the dipole wakefield. Computations used (a) VORPAL [31] and (b) MIT Photonic Bands [28].

Both the damping waveguides and the triangular PhC suffer from low-group-velocity modes. Why then is the damping worse in the Tri-4-Sapphire cavity? The answer lies in the combined characteristics of the damping structure and the central cavity region. Consider the lowest dipole mode in the CLIC cavity. Section II showed that waveguide damping is more effective when the undamped resonant frequency is further above the cutoff frequency. The central cavity dimensions in the CLIC cavity deter-

mine a dipole resonant frequency; thus, the waveguide dimensions are selected such that cutoff is as far below that frequency as possible (without affecting the accelerating mode too much). The gap between the accelerating frequency and the dipole frequency is large enough such that this scheme results in effective dipole damping.

In contrast, the defect region of the Tri-4-Sapphire cavity is (by definition) highly commensurate with the geometry of the surrounding lattice. Furthermore, the mode patterns in Fig. 10 show little electric field energy inside the dielectric, indicating that the removal of the central rod has a small, perturbative effect (compared to modes at the top of the first band, which have most of their field energy concentrated in dielectric). (For an introduction to electromagnetic perturbation theory, see Ref. [33].) As a result, the dipolar defect resonance is at the same frequency as the low-group-velocity lattice mode (or the “cutoff” mode), and is thus poorly damped. Put another way: the creation of the defect weakly perturbs the band-edge lattice mode; therefore, the mode retains a strong presence in the defect. This argument suggests pushing the inner layer of rods closer to the beam axis, which is likely to increase the dipole resonance frequency in the defect above the flat portion of the lattice band and thus increase coupling to higher-group-velocity lattice modes.

The situation may be exacerbated by the impedance mismatch at the outer layer of rods. Because of its low-group-velocity, the lattice mode shown in Fig. 10 may be highly susceptible to reflections off of the transition between lattice and vacuum, effectively increasing its confinement. This transition could be made smoother by slowly decreasing the radii of the rods in outer layers, but would add significantly to the transverse size of the structure.

VI. WAKEFIELDS OF OPTIMIZED HYBRID PHC CAVITIES

In a previous work, 2D simulations showed that some rod arrangements lacking any lattice symmetry (but retaining some rotational symmetry) dramatically reduce the radiative losses of the accelerating mode as compared to lattice arrangements of equal rod count [10]. In this section, we construct and simulate a 3D multicell cavity from a 2D optimized structure by adding conducting iris plates as done with the triangular lattice PhC. A single cell is pictured in Fig. 11 and will be referred to as Opt-18-Sapphire (rods are sapphire).

The 2D optimizations in Ref. [10] ignored the effect of irises; ideally, the 3D cavity would be re-optimized in their presence. The Opt-18-Sapphire cavity in this work has *not* been re-optimized in 3D; such a pursuit is left to future work. Based on the sensitivity study in Ref. [10], we expect only minor rod displacements (from the 2D optimized arrangement) in 3D optimizations given a small perturbative effect due to the irises. See Appendix B for further discussion of the accelerating mode in Opt-18-

Sapphire.

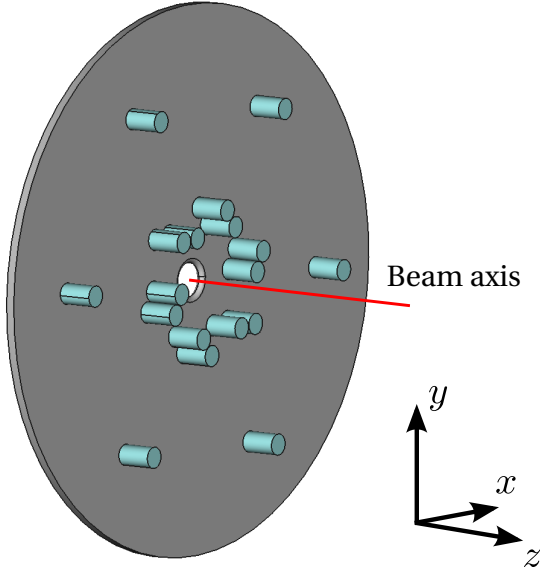


FIG. 11: An optimized hybrid PhC cavity (Opt-18-Sapphire) reduces the number of rods required to confine the accelerating mode.

Simulations in Ref. [18] showed that optimized structures can reduce wakefields; however, the simulations in that study were of single-cell closed cavities (no irises or beam tubes) and made comparisons with only the pill-box. Figures 12–15 detail the wake potentials of an 8-cell Opt-18-Sapphire cavity and compare with CLIC.

Monopole HOMs are more numerous but less prominent in the Opt-18-Sapphire cavity. Transverse wakes in Opt-18-Sapphire are similar to CLIC on average, but *greatly* reduced in comparison with Tri-4-Sapphire (cf. Fig. 7). Unfortunately, the analysis of Section V cannot be applied to Opt-18-Sapphire because of the lack of any band structure; however, these results suggest that non-lattice structures could avoid the inherently poor damping characteristics found in PhC defect cavities.

VII. CONCLUDING REMARKS

Low wakefields require that the energy in HOMs be dissipated as quickly as possible. Thus, a damping mechanism (or structure) should have a mode spectrum without any low group velocities. In principle, the CLIC cavity suffers from low- v_g HOMs near the cutoff frequency of its damping waveguides; however, the sparse mode density of the conducting cavity allowed the placement of the cutoff frequency within an empty region of the spectrum, producing effective damping. PhC cavities suffer from low- v_g -confined HOMs due to the flattening of bands near k -points of strong lattice symmetry. Specifically, in the Tri-4-Sapphire design, the defect-based cav-

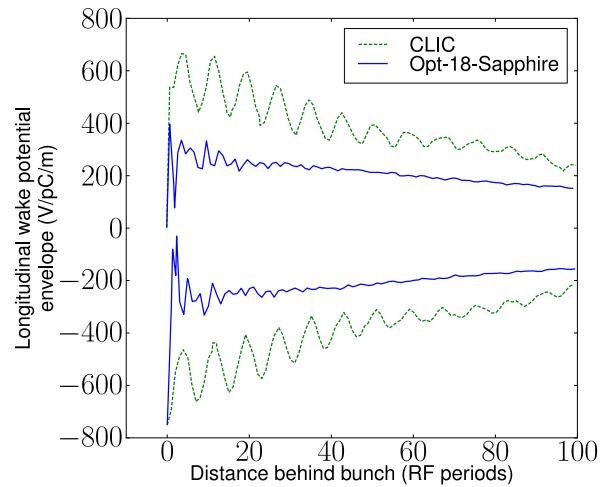


FIG. 12: The monopole wake potential envelope is smoother for the Opt-18-Sapphire cavity. However, the amplitude of the accelerating mode is lower, indicating weaker coupling to the beam (see Appendix B).

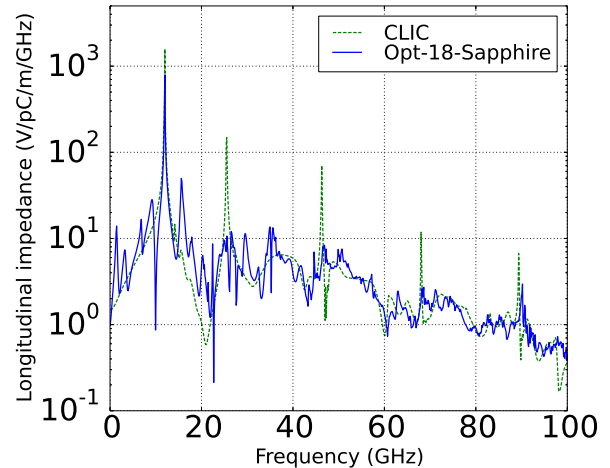


FIG. 13: Monopole HOMs are numerous but suppressed in the Opt-18-Sapphire cavity.

ity supports dipolar resonances that strongly couple to band-edge PhC modes with low- v_g .

Future work should focus on reducing wakefields in lattice-based PhC cavities because the lattice structure has the potential to reduce surface magnetic fields and increase accelerating efficiencies (see Appendix B) and PhC band theory provides an explanation for the existence of troublesome HOMs. Possible routes to reducing wakes in Tri-4-Sapphire cavities include perturbing the central defect region to eliminate low- v_g resonances and/or reducing impedance mismatch at the truncation of the lattice. Given the low wakefields in the Opt-18-Sapphire cavity (and its high Q_{rad} to rod-count ratio), brute-force optimization of rod positions to lower wakefields is also recommended.

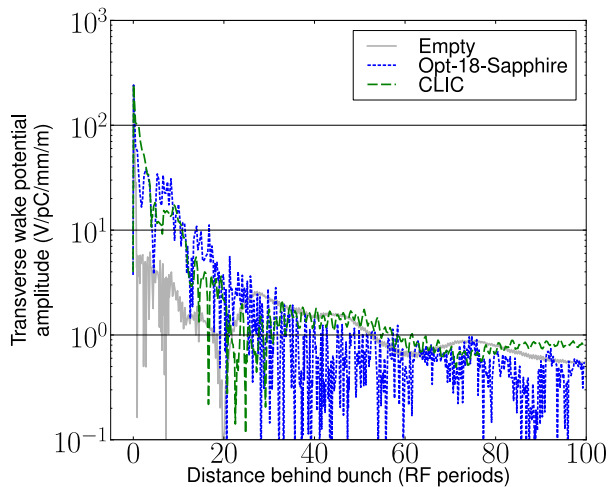


FIG. 14: Optimized 18-rod cavity reduces transverse wakes Transverse dipole wake potentials in 8-cell cavities using conducting absorbers.

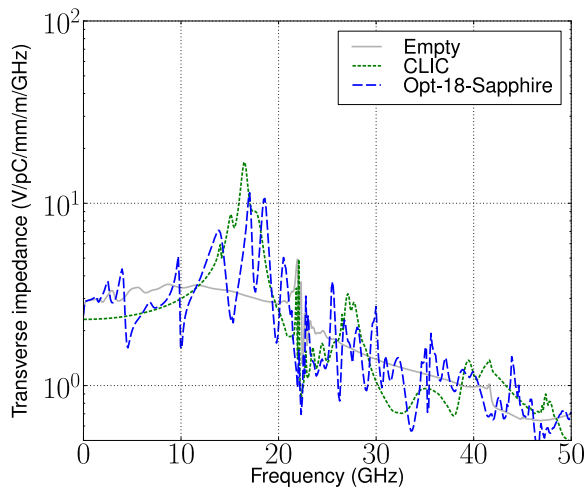


FIG. 15: Transverse dipole impedance in 8-cell cavities using conducting absorbers.

VIII. ACKNOWLEDGMENTS

This work was supported by the U.S. Department of Energy grant DE-FG02-04ER41317.

Most of the simulations described in this work were performed with the VORPAL framework; we would like to acknowledge the efforts of the VORPAL team: D. Alexander, K. Amyx, E. Angle, T. Austin, G. I. Bell, D. L. Bruhwiler, E. Cormier-Michel, Y. Choi, B. M. Cowan, R. K. Crockett, D. A. Dimitrov, M. Durant, B. Jamroz, M. Koch, S. E. Kruger, A. Likhanskii, M. C. Lin, M. Loh, J. Loverich, S. Mahalingam, P. J. Muldowney, C. Nitter, K. Paul, I. Pogorelov, C. Roark, B. T. Schwartz, S. W. Sides, D. N. Smithe, P. H. Stoltz, S. A. Veitser, D. J. Wade-Stein, N. Xiang, C. D. Zhou.

We would also like to thank Alexej Grudiev at CERN

for providing the CLIC cavity geometry.

Appendix A: Absorbers

To absorb wakefields, the ends of each damping waveguide and the transverse edges of the PhC simulations were filled with blocks of conducting material with a special conductivity profile aimed at minimizing reflections off of the cavity-facing surface. The profile is given by

$$\sigma(w) = \sigma_{\max} \left(\frac{w}{W} \right)^2 \quad (\text{A1})$$

where w is depth in the conductor and W is the entire depth of the conducting block. The quadratic form resembles damping techniques used in practice [34], where a cone of absorbing material is placed at the end of a damping waveguide. Our calculations used $W = 25\text{mm}$ and $\sigma_{\max}/\varepsilon_0 = 4.7\omega_{\text{acc}}$ where $\omega_{\text{acc}} = 2\pi 12\text{GHz}$.

We have found that the additional contribution to the wake potentials due to reflections off of the conducting absorbers are higher in the CLIC cavity than in the hybrid PhC cavities. These findings were obtained from simulations with large transverse extents—125mm from beam axis to simulation edge in both x and y (simulations in Section IV had approximately 40mm between the beam axis and the start of the absorbers). Wakefield reflections off of the absorbers at 40mm show up in the wake potential at $s \gtrsim 80\text{mm}$, whereas reflections from 125mm absorbers show up at $s \gtrsim 250\text{mm}$. Transverse dipole wake potential results were compared at distances of $80\text{mm} < s < 250\text{mm}$ (see Fig. 16). Differences in this region were significant for the CLIC cavity and minor in all hybrid PhC cavities. This means wakefield damping can be improved by reducing the impedance mismatch of the absorber in the CLIC waveguides, whereas improving absorption in the PhC cavities will have little impact on the wake potentials.

Appendix B: Accelerating mode comparison

Accelerator cavity design is a complex multidimensional optimization process that tries (in no particular order) (1) to maximize the accelerating electric field (or gradient) so that high energies are reached over short distances, (2) to maximize the transfer of electromagnetic power to the beam, and (3) to minimize wakefields to avoid beam instabilities and breakup. The main body of this paper focused on wakefields in hybrid PhC cavities (i.e. goal (3)). This Appendix addresses some aspects of goals (1) and (2) so that a more complete comparison between the CLIC and hybrid PhC cavities may be drawn.

Using VORPAL, figures of merit for the accelerating mode in each cavity type were calculated and compared for a periodic single cell with iris radius $a = 3.15\text{mm}$, iris thickness $d = 1.67\text{mm}$, and phase advance $\phi = 2\pi/3$ and

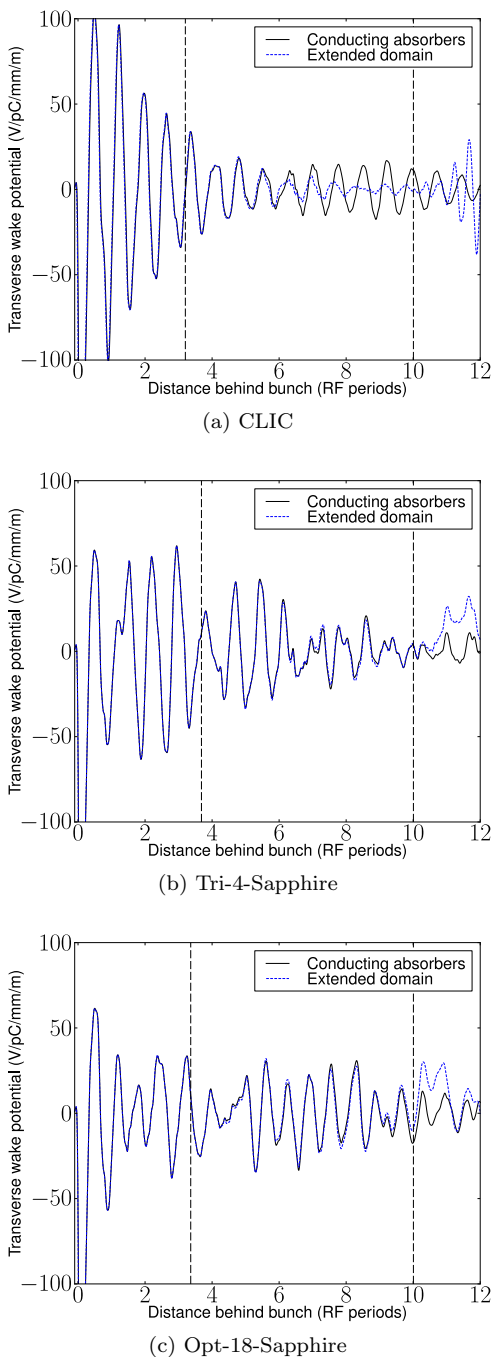


FIG. 16: Reflections off of the conducting absorbers cause differences in the wake potentials between the two vertical lines (more so in the CLIC cavity). Beyond the second line, reflections from the extended domain boundaries reach the beam axis.

are summarized in Table I. The quality factors quantify power losses due to various physical mechanisms;

- Q_{rad} : Losses due to radiation leaking through the truncated PhC structures (confinement of the accelerating mode is not perfect). Applies to hybrid PhC cavities only.

- Q_{metal} : Losses due to RF heating of copper surfaces.
- Q_{diel} : Losses due to RF heating of sapphire rods. Applies to hybrid PhC cavities only. We use a conservative value for the sapphire loss tangent: 10^{-4} .

The shunt impedance per unit length is

$$r_{\text{shunt}} = \frac{V^2}{PL} \quad (\text{B1})$$

where V is the accelerating voltage across a single cell, P is the total power loss per cell, and L is the length of a single cell ($L = 8.33\text{mm}$ based on the synchronicity condition). The accelerating gradient is simply $E_{\text{acc}} = V/L$. The loss factor per unit length is $k = V^2/4UL$ where U is the accelerating mode stored energy. The group velocity of the accelerating mode is v_g , obtained from two simulations at different phase advances.

1. Surface fields

Figures 17 and 18 show the absolute values of E_z and \mathbf{B}_\perp on the z -midplane of the relevant periodic single cell cavities. The z -dependences of the fields are very similar amongst the different cavity types, as expected based on the common iris geometry in each structure. The maximum surface electric field occurs on the iris in all cases, explaining the uniformity of $E_{\text{metal,surf,max}}/E_{\text{acc}}$ across all cavity types. The maximum surface magnetic field occurs on the innermost radial walls of the CLIC cavity; the elliptic curvature of this feature was carefully chosen to minimize $cB_{\text{surf}}/E_{\text{acc}}$.

In the hybrid PhC cavities, $B_{\text{metal,surf,max}}$ occurs where the innermost rods abut the conducting endplates. Since the maximum occurs at the interface between dielectric and conductor, the method used to hold the rods in place will require careful consideration. For example, brazing material could be more prone to breakdown or suffer greater heating losses than copper. The experiment in Ref. [4] successfully secured the rods simply by endplate pressure. On the other hand, covering the region of conductor suffering the maximum magnetic field with dielectric could suppress the breakdown mechanism. Of course, only experiment will tell.

2. Power losses/Accelerating efficiency

The reduced copper surface area in the hybrid PhC cavities lowers copper heating losses compared to CLIC and the pillbox; however, (unlike the all-copper cavities) dielectric heating and radiative losses play a role. The shunt impedance is a strong indicator of accelerating efficiency, and is higher in the CLIC cavity. However, shunt impedances in the hybrid PhC cavities could be increased by reducing radiative losses (e.g. by adding more layers

TABLE I: Figures of merit for the accelerating mode in periodic single cell cavities. $a = 3.15\text{mm}$, $d = 1.67\text{mm}$, $\phi = 2\pi/3$. All simulations performed at $\Delta z/d = 8$.

	Pillbox	CLIC	Tri-4-Sapphire	Opt-18-Sapphire
v_g/c (%)	1.83	1.65	1.16	0.78
Q_{metal}	6,700	5,900	11,400	11,400
Q_{rad}	∞	∞	26,600	3,800
Q_{diel}	∞	∞	67,000	39,000
Q_{total}	6,700	5,900	7,100	2,700
r_{shunt} ($\text{M}\Omega/\text{m}$)	106	82	70	18
k ($\text{V}/\text{pC}/\text{m}$)	298	260	187	125
$E_{\text{surf,metal,max}}/E_{\text{acc}}$	1.93	1.96	1.93	1.93
$cB_{\text{surf,metal,max}}/E_{\text{acc}}$	1.0	1.54	1.49	1.73
$E_{\text{surf,diel,max}}/E_{\text{acc}}$	—	—	0.54	0.64
$cB_{\text{surf,diel,max}}/E_{\text{acc}}$	—	—	1.26	1.79
$E_{\text{diel,max}}/E_{\text{acc}}$	—	—	0.60	0.79

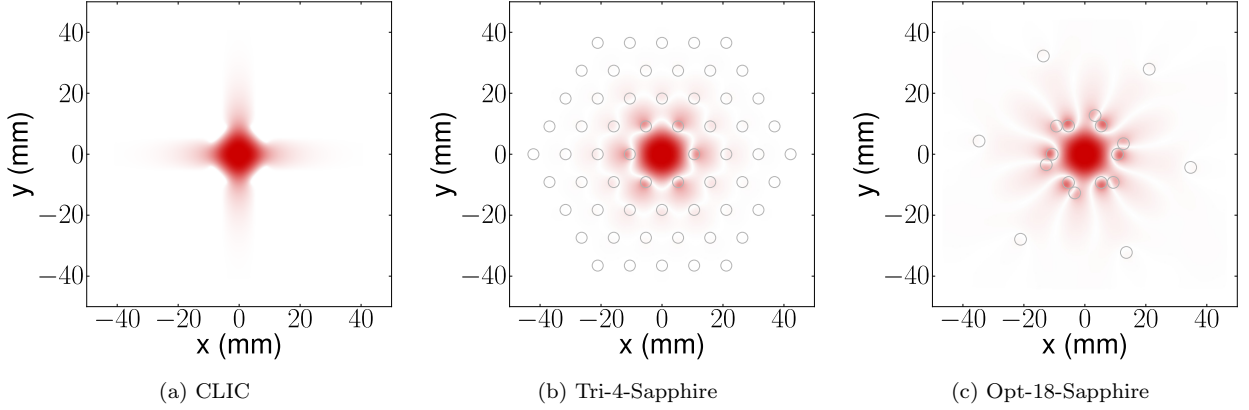


FIG. 17: Absolute value of E_z on the midplane (in z) of periodic single cell cavities.

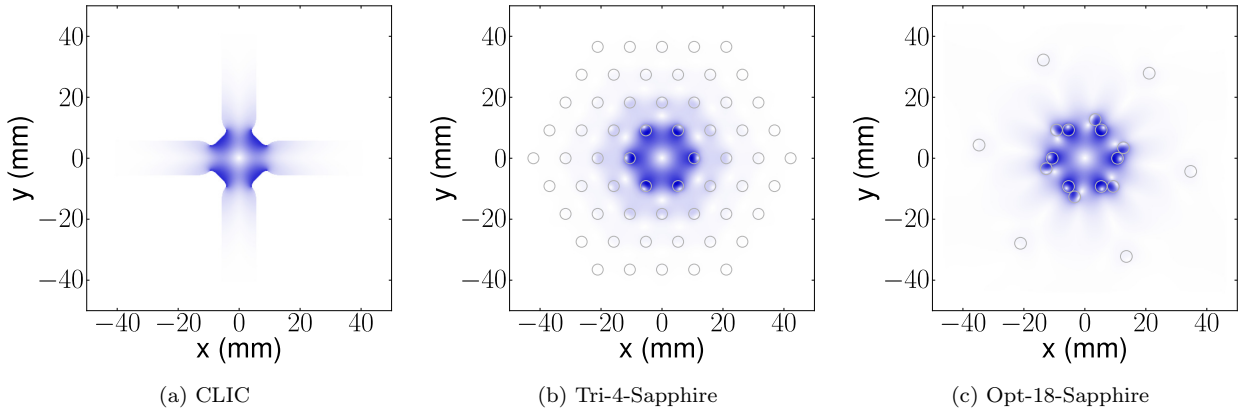


FIG. 18: Absolute value of \mathbf{B}_{\perp} on the midplane (in z) of periodic single cell cavities.

TABLE II: Hypothetical accelerating mode figures of merit for the Tri-6-Sapphire cavity and the Opt-18-Sapphire cavity (given that 3D optimizations reproduce 2D Q_{rad} values). Values in Table I not appearing here are assumed to be the same.

	Pillbox	CLIC	Tri-6-Sapphire	Opt-18-Sapphire
Q_{metal}	6,700	5,900	11,400	11,400
Q_{rad}	∞	∞	2,400,000	25,000
Q_{diel}	∞	∞	67,000	39,000
Q_{total}	6,700	5,900	9,700	6,500
r_{shunt} (M Ω /m)	106	82	97	43

of rods to the Tri-4-Sapphire cavity, or performing optimizations in 3D on the Opt-18-Sapphire cavity as discussed below).

In the optimized cavity, Q_{rad} is very sensitive to structural perturbations (cf. Ref. [10]). We find that the beam tubes in the 3D Opt-18-Sapphire cavity drop Q_{rad} by nearly an order of magnitude relative to the 2D value reported in Ref. [10] (from 25,000 in 2D to 3,800 in 3D with beam tubes). It remains to be seen whether further optimization in 3D can regain the original 2D Q_{rad} . The Q_{rad} of the Tri-4-Sapphire cavity is the same in 2D, indicating some robustness of the confinement to structural perturbations.

Table II shows projected figures of merit under the following assumptions: (1) a 3D optimization of the Opt-18-Sapphire cavity (involving only minor repositioning of the rods) restores the 2D Q_{rad} (25,000), (2) two layers of rods are added to the Tri-4-Sapphire cavity (making Tri-6-Sapphire) basically eliminating radiative losses, and (3) the stored energy, surface fields, and voltage gain remain the same in each (a safe assumption if the fields are only slightly perturbed). Of the cavities with wakefield damping, this gives the Tri-6-Sapphire cavity the largest shunt impedance; however, increasing the number of lattice layers could increase wakefields.

-
- [1] E. Colby, in *AIP Conference Proceedings* (IOP INSTITUTE OF PHYSICS PUBLISHING LTD, 2002), pp. 39–46, ISSN 0094-243X.
- [2] D. R. Smith, D. Li, D. C. Vier, N. Kroll, and S. Schultz, in *Advanced Accelerator Concepts* (1997), vol. 398 AIP Conf. Proc., pp. 518–527.
- [3] N. Kroll, D. R. Smith, and S. Schultz, in *Advanced Accelerator Concepts* (1993), vol. 279 AIP Conf. Proc., pp. 197–211.
- [4] M. R. Masullo, A. Andreone, E. Di Gennaro, S. Albanese, F. Francomacaro, M. Panniello, V. G. Vaccaro, and G. Lamura, *Microwave and Opt. Tech. Lett.* **48**, 2486 (2006).
- [5] E. Gennaro, C. Zannini, S. Savo, A. Andreone, M. Masullo, G. Castaldi, I. Gallina, and V. Galdi, *New Journal of Physics* **11**, 113022 (2009).
- [6] E. Di Gennaro, S. Savo, A. Andreone, V. Galdi, G. Castaldi, V. Pierro, and M. Masullo, *Applied Physics Letters* **93**, 164102 (2008).
- [7] M. Shapiro, E. Smirnova, C. Chen, and R. Temkin, in *Particle Accelerator Conference, 2003. PAC 2003. Proceedings of the* (IEEE, 2004), vol. 2, pp. 1255–1257, ISBN 0780377389, ISSN 1088-9299.
- [8] E. I. Smirnova, A. S. Kesar, I. Mastovsky, M. A. Shapiro, and R. J. Temkin, *Phys. Rev. Lett.* **95**, 074801 (2005).
- [9] R. A. Marsh, M. A. Shapiro, R. J. Temkin, V. A. Dolgashev, L. L. Laurent, J. R. Lewandowski, A. D. Yermian, and S. G. Tantawi, *Phys. Rev. ST Accel. Beams* **14**, 021301 (2011).
- [10] C. Bauer, G. Werner, and J. Cary, *Journal of Applied Physics* **104**, 053107 (2008).
- [11] B. Cowan, *Physical Review Special Topics-Accelerators and Beams* **11**, 011301 (2008).
- [12] X. Lin, *Physical Review Special Topics-Accelerators and Beams* **4**, 051301 (2001).
- [13] M. Thompson, H. Badakov, A. Cook, J. Rosenzweig, R. Tikhoplav, G. Travish, I. Blumenfeld, M. Hogan, R. Ischebeck, N. Kirby, et al., *Physical review letters* **100**, 214801 (2008), ISSN 1079-7114.
- [14] N. Bloembergen, *Quantum Electronics, IEEE Journal of* **10**, 375 (1974), ISSN 0018-9197.
- [15] D. Du, X. Liu, G. Korn, J. Squier, and G. Mourou, *Applied Physics Letters* **64**, 3071 (1994).
- [16] J. Power, W. Gai, S. Gold, A. Kinkead, R. Konecny, C. Jing, W. Liu, and Z. Yusof, *Physical review letters* **92**, 164801 (2004), ISSN 1079-7114.
- [17] C. Jing, W. Gai, J. Power, R. Konecny, W. Liu, S. Gold, A. Kinkead, S. Tantawi, V. Dolgashev, and A. Kanareykin, *Plasma Science, IEEE Transactions on* **38**, 1354 (2010).
- [18] G. R. Werner, C. A. Bauer, and J. R. Cary, *Phys. Rev. ST Accel. Beams* **12**, 071301 (2009), URL <http://link.aps.org/doi/10.1103/PhysRevSTAB.12.071301>.
- [19] R. A. Marsh, Ph.D. thesis, Massachusetts Institute of Technology (2009).
- [20] C. Jing, F. Gao, S. Antipov, Z. Yusof, M. Conde, J. G. Power, P. Xu, S. Zheng, H. Chen, C. Tang, et al., *Phys. Rev. ST Accel. Beams* **12**, 121302 (2009), URL <http://link.aps.org/doi/10.1103/PhysRevSTAB.12.121302>.
- [21] I. Wilson and W. Wuensch, *Arxiv preprint physics/0008101* (2000).
- [22] A. Grudiev and W. Wuensch, *Proceedings LINAC2004* (2004).
- [23] H. Braun, R. Corsini, J. P. Delahaye, A. de Roeck, S. Dbert, A. Ferrari, G. Geschonke, A. Grudiev, C. Hauviller, B. Jeanneret, et al. (2008).
- [24] A. Grudiev (2012), private communication.
- [25] A. Grudiev (2009), cLIC-ACE.

- [26] N. Kroll and X. Lin, in *Particle Accelerator Conference, 1993., Proceedings of the 1993* (IEEE, 1993), pp. 3453–3455.
- [27] X. Lin and N. Kroll, in *Particle Accelerator Conference, 1995., Proceedings of the 1995* (IEEE, 1995), vol. 3, pp. 1809–1811.
- [28] S. G. Johnson and J. D. Joannopoulos, *Opt. Express* **8**, 173 (2001), URL <http://www.opticsexpress.org/abstract.cfm?URI=OPEX-8-3-173>.
- [29] D. Li, N. Kroll, D. Smith, and S. Schultz, in *AIP Conference Proceedings* (1997), vol. 398, p. 528.
- [30] P. B. Wilson, Tech. Rep. SLAC-PUB-4547, SLAC (1989).
- [31] C. Nieter and J. R. Cary, *J. Comput. Phys.* **196**, 448 (2004).
- [32] O. Napoly et al., *Nuclear Instruments and Methods in Physics Research Section A: Accelerators, Spectrometers, Detectors and Associated Equipment* **334**, 255 (1993), ISSN 0168-9002.
- [33] J. D. Joannopoulos, S. G. Johnson, J. N. Winn, and R. D. Meade, *Photonic crystals: molding the flow of light* (Princeton university press, 2011).
- [34] M. Luong, I. Wilson, and W. Wuensch, in *Particle Accelerator Conference, 1999. Proceedings of the 1999* (IEEE, 1999), vol. 2, pp. 821–823.